Journal of Materials Chemistry A

Accepted Manuscript

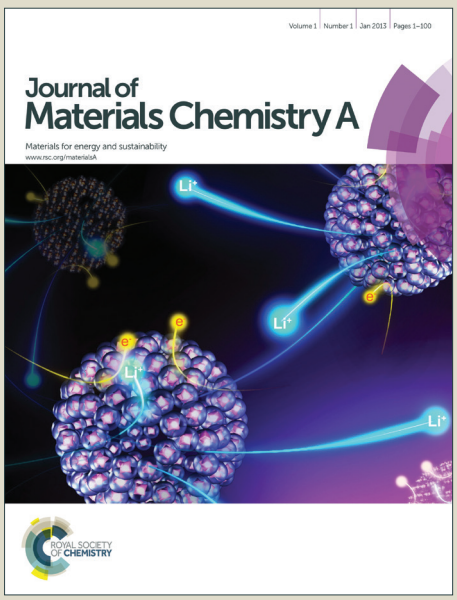

ROYAL SOCIETY OF CHEMISTRY

www.rsc.org/materialsA

Journal Name

ARTICLE

Space-confined growth of Ag_3PO_4 nanoparticles within WS_2 sheets: Ag_3PO_4 /WS_2 composite as a visible-light-driven photocatalyst for decomposing dyes

Received 00th January 20xx,
Accepted 00th January 20xx

DOI: 10.1039/x0xx00000x

www.rsc.org/

Yu Hongjian[a], Yu Yong[b] , Liu Jianghao[c] , Ma Peiyan[b,*], Wang Yucheng[a], Zhang Fan[a] and Fu Zhengyi[a,*]

A highly efficient Ag_3PO_4/WS_2 composite photocatalyst was synthesized by controlling the growth of Ag_3PO_4 nanoparticles within WS_2 sheets. The process can tune the microstructure, stability and visible-light photocatalytic performance of Ag_3PO_4. The WS_2 sheets, possessing uncoordinated sulfur atoms on exposed surfaces and edges, play an important role in the formation of Ag_3PO_4/WS_2 composite. With 0.05mol of AgAc added, the Ag_3PO_4/WS_2 composite shows the highest photocatalytic activity. The matched energy level between Ag_3PO_4 and WS_2 inhibits the recombination of the photogenerated electrons and holes. The enhanced photocatalytic activity is also attributed to the multi-interface heterojunction structure assembled by two-dimensional sheets and nanoparticles, driven by the chemical binding. The addition of WS_2 sheets can also reduce the rate at which Ag^+ dissolves from Ag_3PO_4 into the water, improving the stability of Ag_3PO_4. This work could provide new insights into fabricating highly efficient and stable Ag_3PO_4–transition-metal dichalcogenide composite photocatalysts for dye degradation.

Introduction

Since the proposal of photocatalytic technology by Fujishima in 1972, great efforts have been directed toward the exploration of visible-light-driven photocatalysts with broad spectral ranges and low electron-hole recombination rate for the purpose of treating water pollution [1-3]. In recent years, Ag_3PO_4 has been considered a representative visible-light-driven photocatalyst that performs better than N doped TiO_2 and other photocatalysts in many aspects [4]. Many groups have tried to regulate the microstructure, control the high-energy crystal faces [5] , design Ag_3PO_4-based composite materials [6] , and reveal the catalytic mechanism [7]. However, without the support of carriers, nano Ag_3PO_4 particles derived from ion exchange tend to spontaneously form agglomerates. As a consequence, the specific surface area is significantly reduced and a great many active sites disappear. Besides, the rate of photoinduced electron-hole recombination of Ag_3PO_4 is still high. Therefore, effective measures are required to regulate the microstructure and improve the performance of Ag_3PO_4 crystals.

Designing heterogeneous photocatalysts in which built-in electric field is the major driving force for the separation of photoinduced charge has been demonstrated to be an effective strategy of improving catalytic performance. For the nano-scale heterogeneous system, interface control is a key factor in strengthening the interface properties of materials. Heterogeneous photocatalysts based on two-dimensional graphene or graphene-like materials have shown a remarkably interface enhancement effect due to high interfacial area, abundant active sites, wide space charge region, and short path length of electron transmission. For example，Xiaofei Yang[8] and Santosh Kuma[9] prepared Ag_3PO_4/graphene and Ag_3PO_4/g-C_3N_4 composites, respectively, in which the photo induced electron-hole pairs can be separated effectively and the photocatalytic performance of Ag_3PO_4 is improved.

Additionally, two-dimensional materials have proven to be effective in restricting the size of particles down to the nano scale, and restraining the agglomeration of nanoparticles. For example, the alternately intercalated monolayered vanadium oxide and graphene frameworks show emergent magnetocaloric effect [10]. The space-confined growth of MoS_2 nano sheets within graphene leads to excellent catalytic activity for hydrogen evolution reaction [11].

With the upsurge of interest in graphene-based materials, graphene-like layered transition metal chalcogenide ML_2 (M = Mo, W; L = S, Se, Te) compounds have been given more attention. Monolayer or few layer stacked ML_2 can be obtained by liquid exfoliation technology or other means, giving the materials some special properties and enabling applications in the areas of catalysts, transistors, lubricants[12], hydrogen storage, batteries and supercapacitors[13-17]. For

[a] State Key Lab of Advanced Technology for Materials Synthesis and Processing, Wuhan University of Technology, Wuhan, Hubei 430070, PR China.
[b] School of Chemistry , Chemical engineering and Life science, Wuhan University of Technology, Wuhan, Hubei 430070, PR China.
[c] The State Key Laboratory of Refractories and Metallurgy, Wuhan University of Science and Technology, Wuhan 430081, China.
E-mail: mapeiyan@whut.edu.cn, fuzhengyi@whut.edu.cn.
Electronic Supplementary Information (ESI) available: See DOI: 10.1039/x0xx00000x

example, bulk WS_2 is an indirect band-gap semiconductor. Nevertheless, monolayer WS_2 is found to be a semiconductor with a bandgap of 1.9 eV, which is a promising photocatalytic material. Additionally, it is a favorable carrier for nano-scale photocatalysts, owing to its good chemical stability. Despite these exploratory findings, the critical problems concerning the interaction between ML_2 and photocatalysts, and the influence of interfacial microstructure on the performance of the heterogeneous materials need to be explored further.

In the present work, we prepared Ag_3PO_4/WS_2 heterogeneous photocatalysts by confining Ag_3PO_4 nanoparticles within WS_2 sheets in aqueous solution. In this process, Ag_3PO_4 nanoparticles are evenly dispersed on the surface of few-layer WS_2 sheets. The driving force of the formation of Ag_3PO_4/WS_2 heterogeneous structure without any linking reagent is discussed in detail. The results indicate that WS_2 sheets can significantly improve the photocatalytic activity of Ag_3PO_4 due to the energy level match between Ag_3PO_4 and WS_2 by facilitating the separation of hole-electron pairs.

Experimental Section

Synthesis of Ag_3PO_4-WS_2 Composite

Few-layer WS_2 aqueous solution was prepared by the mechanical exfoliation method reported by Jonathan N. Coleman [18]. In the present experiment, 0.01g of bulk WS_2 powder was first mixed with 50 ml of deionized water, and then transferred to a high-power ultrasonic device where the exfoliation process lasted for 6h before the supernatant was collected. Then a certain amount of silver acetate was dispersed into the WS_2 aqueous solution with uninterrupted agitation for 0.5h at room temperature. Afterward, 15ml of Na_3PO_4 solution was added drop by drop. The molar ratio of silver acetate to Na_3PO_4 was fixed to be 3:1. The mixture was continuously stirred for 0.5h. Lastly, the obtained Ag_3PO_4/WS_2 composite was washed with deionized water and ethanol alternatively, then dried at 60℃ under vacuum. Different Ag_3PO_4/WS_2 composites were prepared with 0.005, 0.01, and 0.016mol silver acetate as Ag source. The samples were labeled as AW0.005, AW0.01 and AW0.016, respectively. For comparison, pure Ag_3PO_4 particles were synthesized by direct reaction of 30mL of CH_3COOAg (0.0048M) with 10ml of 0.012M Na_3PO_4 solution. Few-layer stacked WS_2 aqueous solution was freeze-dried to obtain a bare WS_2 sample.

Characterization

X-ray diffraction (XRD) patterns related to the phase structure of samples were obtained using a Rigaku D/max-III A diffractometer. The morphologies of the different samples were observed using a JSM-5610LV scanning electron microscope (SEM) and Hitachi H-800 transmission electron microscope (TEM). UV-vis diffuse reflectance spectra were obtained from a UV2550 spectrophotometer. X-ray photoelectron spectra were obtained to analyze the composition of the composites on an ESCALABMK II X-ray photoelectron spectrometer (XPS).

Photocatalytic Experiment

A 350W Xe lamp equipped with a cutoff filter (λ>420 nm) was used as the light source in the photocatalytic experiments. Twenty mg of photocatalyst was dispersed into 20ml of Rhodamine B (RhB) (10^{-5}mol/L) or phenol solution (20mg/L). Then the mixture was stirred in darkness for 30min to attain the absorption-desorption equilibrium. At regular time intervals, 5 ml of the mixture was taken out and centrifuged to separate the supernatant, which was analyzed using UV-vis absorption spectra at 554 nm.

Cycling experiments were conducted to evaluate the stability of the Ag_3PO_4 /WS_2 composite. After each cycle, the samples were washed with deionized water and added to fresh RhB solution, followed by another cycle. Samples of Ag_3PO_4 /WS_2 composites were also kept for 6 months to assess its stability (photosensitivity).

Furthermore, comparative photocatalysis experiments were conducted to explore the catalytic mechanism, in which p-benzoquinone (BZQ), disodium ethylene diamine tetra-acetate (Na_2-EDTA) and tert-butanol were added respectively to RhB solution with other conditions unchanged.

Result and discussion

Characterization

Our design concept for the Ag_3PO_4/WS_2 composite is to use the homogeneous WS_2 solution to restrain the growth of the nano Ag_3PO_4. First, silver ions added into WS_2 sheet solution are adsorbed on the surface of the two-dimensional sheets. Second, phosphate anions are introduced to react with silver ions. Lastly, Ag_3PO_4 crystals nucleate and grow in the micro environment created by the WS_2 sheet solution. Therefore, the obtained composite consists of uniformly-distributed Ag_3PO_4 and WS_2. Additionally, WS_2 sheets with limited layers are expected to protect Ag_3PO_4 from dissolution in water. A diagram of the preparation procedure appears in Fig. 1.

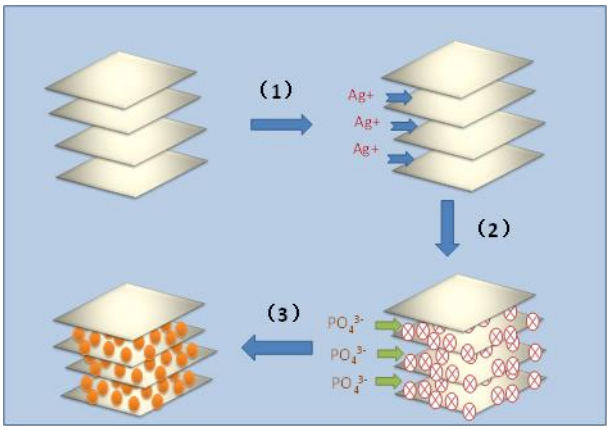

Fig.1. Diagram of space-confined growth of Ag_3PO_4 nanoparticles within WS_2 sheets. (1) WS_2 sheets adsorb silver ions from the solution ; (2) phosphate anions react with the silver ions on the surface of WS_2 sheets; (3) Ag_3PO_4 nanoparticles nucleate and grow among the WS_2 sheets.

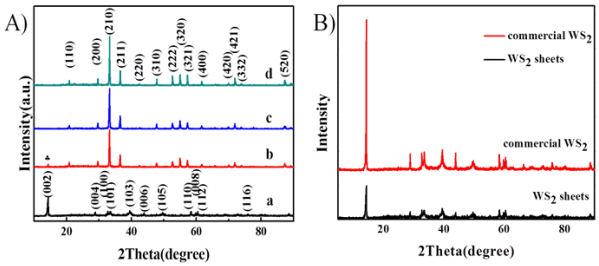

Fig. 2 A) XRD patterns of (a) bare WS_2 sheets, (b) AW0.005, (c) AW0.01 and (d) AW0.016. B) XRD patterns of commercial WS_2 (bulk) and bare WS_2 sheets.

Fig. 2a shows the XRD pattern of bare WS_2 sheets. The diffraction peaks correspond to the hexagonal phase of 2H-WS_2 (JCPDS No.08-0237), indicative of well-resolved crystallized WS_2 sheets obtained by direct exfoliation technology. A weak peak at 2Θ=14.50 is indexed to the (002) plane, which is apparently lower than that of commercial WS_2 powder (Fig.2B). However, we believe the peak intensity is influenced by the preparation procedure of the sample for XRD measurement, which results in restacking WS_2 sheets. For the sample of AW0.05 (Fig. 2b), the XRD pattern confirms the formation of WS_2/Ag_3PO_4 composite. The intensity of the (002) plane of WS_2 sheets, marked by a club symbol, is weaker than that of bare WS_2 sheets, indicating the intercalation of Ag_3PO_4 into WS_2 sheets. The other diffraction peaks can be assigned to the body-centered Ag_3PO_4 (JCPDS No.06-0505). In addition, if more silver acetate is added, the intensity of diffraction peaks of Ag_3PO_4 is enhanced accordingly in the cases of AW0.05, AW0.01 and AW0.016. However, as can be observed from the patterns of AW0.01 and AW0.016 (Fig. 2c and 2d), the (002) planes of WS_2 sheets disappear in these cases, due to the incorporation of more Ag_3PO_4 particles in the reaction process. Similar phenomena have been observed in the system of graphene moderated nanoparticles[19].

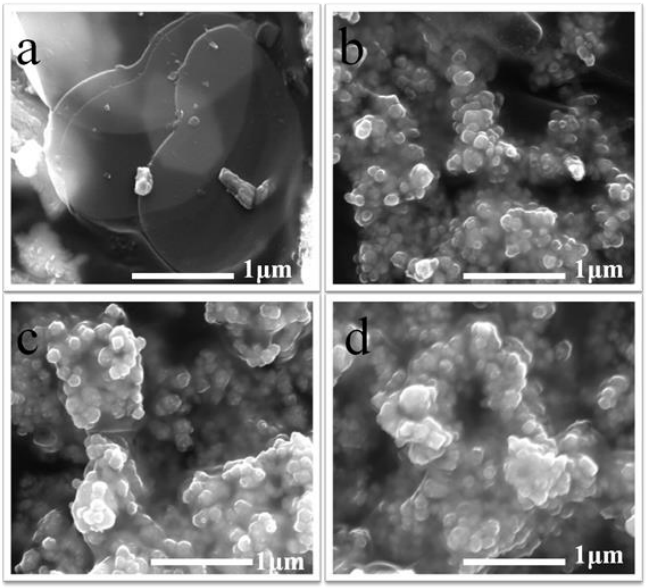

Fig. 3 FESEM images of (a) bare WS_2 sheets, (b) AW0.005, (c) AW0.01 and (d) AW0.016.

A typical FESEM image (Fig. 3a) shows that transparent WS_2 sheets with smooth surface can be synthesized successfully in high yields with uniform thickness and micrometer size. Figs. 3b-3d exhibit the images of AW0.005, AW0.01 and AW0.016 composites, respectively, in which homogeneous Ag_3PO_4 particles with an average size of less than 100nm are enwrapped by WS_2 sheets, indicating the excellent flexibility of few-layer WS_2 substrate, as well as the intimate contact between WS_2 sheets and nano Ag_3PO_4 particles. Fig.S1 verifies the layer by layer structure consisted of nano Ag_3PO_4 particles and WS_2 sheets .Therefore, the self–accumulating phenomenon of nano Ag_3PO_4 particles is inhibited. At the same time, the immobilization of the nanoparticles on the two-dimensional sheets generates a high interfacial area and abundant active sites, which are the desirable characteristics of a multi-interface heterojunction structure and favorable factors for dye degradation. Accordingly, WS_2 sheets could be utilized as an effective support for in-situ nucleation and growth of nano Ag_3PO_4 particles without any additives. We also observe that nano Ag_3PO_4 particles attached on the surface of two-dimensional WS_2 sheets display a different morphology from that of the pure Ag_3PO_4 sample with irregular morphology and larger size (Fig.S2). Therefore, the intercalation of nano Ag_3PO_4 particles restrains the WS_2 sheets from stacking and in turn the microenvironment among WS_2 sheets restricts the growth and aggregation of Ag_3PO_4 particles. According to the XRD and SEM results, a conclusion is obtained that WS_2 sheets play an important role in regulating the microstructure and composition of the Ag_3PO_4/WS_2 composites.

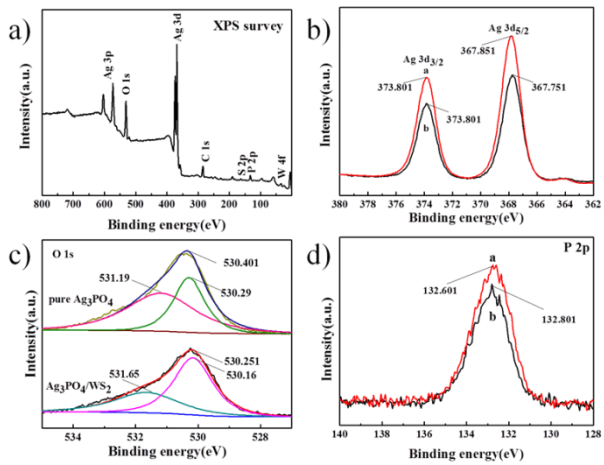

Fig. 4 a) XPS survey spectrum of AW0.01 composite. High-resolution XPS spectrum of b) Ag 3d, c) O 1S, and d) P 2P spectrum of AW0.01 and pure Ag_3PO_4. a and b represent the curves of pure Ag_3PO_4 and Ag_3PO_4/WS_2 composite (AW0.01).

Furthermore, to analyze the interaction between nano Ag_3PO_4 particles and WS_2 sheets, AW0.01, a representative sample, was characterized by XPS. Pure Ag_3PO_4 served as the reference. The full XPS spectrum indicates that AW0.01 is composed of Ag, O, P, S and W (Fig.4a). The XPS peak of C 1s at

284.8 eV is assigned to residual carbon from the XPS instrument. Observed from the high-resolution XPS spectrum of W, two distinct peaks, located at binding energies of 35.506 eV for W 4f5/2 and 33.101eV for W 4f7/2, are very consistent with the characteristic of W^{4+} in WS_2 (Fig.S3)[20]. The XPS spectrum of S2p exhibits a doublet at 162.33 and 163.54 eV, which is the feature of S^{2-} in WS_2 (Fig.S4). The Ag 3d3/2 and Ag 3d5/2 peaks located at 373.801eV and 367.751eV, respectively, correspond to Ag^+ in Ag_3PO_4, showing 0.1eV deviation of 3d5/2 relative to the value in pure Ag_3PO_4 (Fig.4b)[21]. The binding energy of O1s (structural oxygen) in Ag_3PO_4/WS_2 is located at 530.16eV, indicating a trend to move to the lower binding energy in comparison with the datum in pure Ag_3PO_4 (Fig. 4c). The binding energy of P 2p corresponding to P^{5+} in Ag_3PO_4 shows an increase of 0.2eV after the combination of WS_2 with Ag_3PO_4(Fig.4d). The variations of binding energy of Ag 3d, P 2p and O1s are attributed to the covalent bonding between WS_2 and Ag_3PO_4. In previous studies, the unsaturated S atoms were found to play important roles in the catalytic process[22]. These S atoms located at the edge and the exposed surface of the WS_2 sheets are active, giving the sheets a strong ability to attract Ag^+ in the solution, which results in the in-situ formation of nano Ag_3PO_4 particles on the surface of WS_2 sheets. Nevertheless, this induction force is not strong enough to form Ag_2S, which is verified by above-mentioned XRD results. The close contact between WS_2 and Ag_3PO_4 contributes to inhibiting Ag_3PO_4 from detaching into the water, thereby protecting its activity.

Raman spectra were utilized to further examine the interaction of WS_2 nanosheets and nano Ag_3PO_4. Several peaks at the range of 500-1300 cm^{-1} correspond to the vibrations of Ag_3PO_4.The WS_2 nanosheets exhibit first-order modes at approximately 345.919 and 414.677 cm^{-1}, corresponding to the E_{2g}^1 and A_{1g} modes from in-plane and out-of-plane vibrations, respectively(Fig.S5). The relative peak intensity ratio (E_{2g}^1/A_{1g}) is higher than 1.0, indicating the limited layer numbers of WS_2[23]. For AW0.01 , the decrease in peak intensity ratio (E_{2g}^1/A_{1g}) of WS_2 is due to the incorporation of nano Ag_3PO_4. Compared with the pure WS_2 sheets, the E_{2g}^1 and A_{1g} shift to higher values, which indicates the close interaction between Ag_3PO_4 and WS_2 .

Figure S6 shows the FTIR results of pure Ag_3PO_4,WS_2 sheets and AW0.01. For WS_2 sheets (Fig.S6a), W-S stretching vibration is observed at 438cm^{-1}. For pure Ag_3PO_4 (Fig.S6b), the peaks at 874 and 1012 cm^{-1} are due to the symmetric and asymmetric stretching vibration of P-O-P rings[24]. The peak at 413 cm^{-1} corresponds to Ag-O stretching vibration. After being coupled with WS_2 sheets (Fig.S6c), the wavenumbers of P-O-P rings shift to lower values, while that of Ag-O stretching vibration shifts to higher value. The shift results from the presence of WS_2 sheets.

The UV-visible diffuse reflectance spectra of bare WS_2 sheets and AW0.01 are shown in Fig.5. For bare WS_2 sheets, there are characteristic absorption peaks at around 444nm, 515nm and 617nm, in the visible-light range and a strong absorption peak at 250nmin the UV-light range. For the sample of AW0.01, there is a characteristic peak located at 450nm, and a broad peak appears in the range of 530-700nm, corresponding to the absorption of Ag_3PO_4 [25], and WS_2, respectively. Compared with the datum of pure Ag_3PO_4 (Fig.S7), the introduction of narrow-gap WS_2 sheets extends the adsorption region and improves the light harvesting efficiency of Ag_3PO_4 in the visible-light range. Additionally, the band gap of WS_2 sheets is calculated to be about 1.9eV, according to the UV-visible diffuse reflectance spectrum of bare WS_2 sheets.

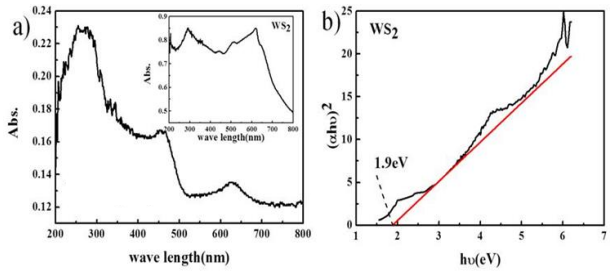

Fig. 5 (a) UV-vis diffusive reflectance spectrum of AW0.01; inset is the UV-vis diffusive reflectance spectrum of bare WS_2 sheets; (b) Calculation of the bandgap of WS_2 sheets based on the $(\alpha h\nu)^2$-hv curve.

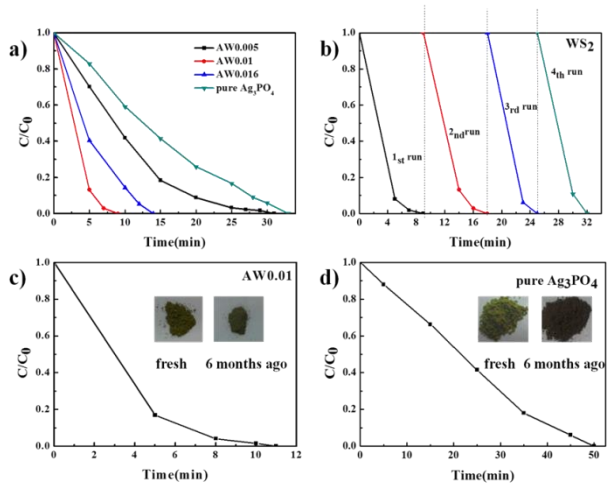

Fig. 6 a) Photocatalytic degradation of RhB solution over the as-prepared Ag_3PO_4/WS_2 composite, bare WS_2 sheets and pure Ag_3PO_4; b) Repeated degradation of RhB solution over recycled AW0.01 photocatalyst under visible light; (c) Photocatalytic degradation of RhB solution over AW0.01 and pure Ag_3PO_4 prepared six months earlier, respectively. Insets in Figures 6c and 6d are pictures of catalyst powder.

Photocatalytic Results and Analysis

The photocatalytic performance of the as-prepared Ag_3PO_4/WS_2 composites and pure Ag_3PO_4 particles were measured by degrading RhB dyes under visible-light irradiation. Fig.6a depicts the change of RhB dye concentration as a function of exposure time to visible light in the presence of different catalysts. Bare WS_2 sheets adsorb 80% of the dye within 100min, indicating favorable adsorption performance and a strong affinity to organic dyes (Fig.S8a). However, its

catalytic activity under visible light is negligible. Pure Ag_3PO_4 can completely decompose the dye after 33min. AW0.005, AW0.01, and AW0.016 show better photocatalytic activity than pure Ag_3PO_4, completing the degradation process in 30, 9, and 14min, respectively. The result indicates that the participation of WS_2 sheets can significantly improve the photocatalytic activity of Ag_3PO_4. Notably, AW0.01 performs best, implying the photocatalytic activity of the composite depends on the appropriate molar ratio of Ag_3PO_4 to WS_2 sheets. In view of negligible degradation effect of bare WS_2 sheets, the enhanced photocatalytic activity is attributed to the excellent adsorption performance of WS_2, as well as the favorable interaction of WS_2 sheets and Ag_3PO_4. AW0.01 has a BET surface area of 5.9518 m^2/g. Therefore, the adsorption performance and enhanced photocatalytic activity are unrelated to the BET surface area. They depend on the essence of the composite materials.

AW0.01 also exhibits the enhanced photocatalytic activity on the degradation of phenol than pure Ag_3PO_4 under visible light, which further verifies the excellent photocatalytic properties of Ag_3PO_4/WS_2 composites(Fig. S9).

The photocatalytic stability of AW0.01 was investigated by recycling it in repeated RhB degradation experiments, as shown in Fig.6b. The photocatalytic activity of AW0.01 remains stable in the first two cycles, after which there is a slight increase in the third and fourth cycles. To further understand the reasons for this phenomenon, the sample collected after four cycling experiments was characterized by XRD measurement (Fig.S8b). It can be seen that the collected sample contains Ag, which results in the slight increase in the photocatalytic activity, due to surface plasmon resonance of Ag [26]. From what has been observed, it can be concluded that the photocatalytic activity of as-prepared composite is kept after several applications, exceeding the stability of pure Ag_3PO_4[27].

The stability of the samples was also tested by utilizing AW0.01 and pure Ag_3PO_4 that had been obtained as catalysts 6 months ago. As can be seen from Fig.6c, AW0.01 keeps its green color and its catalytic ability with negligible loss. For pure Ag_3PO_4, the color changes from yellow to black and the time for degrading dyes extends to 50min, a sharp drop of catalytic ability (Fig.6d). Fig.S10 shows the XRD pattern of AW0.01 prepared 6 month ago. The result indicates that the sample is stable and no metallic Ag is produced after 6-months storage. Based on the above results, we see that the introduction of WS_2 sheets can improve the stability of Ag_3PO_4 in the photocatalytic process and prolong its storage time.

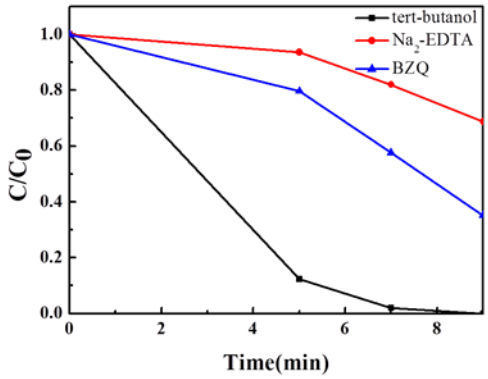

Fig. 7 Photocatalytic degradation curves of RhB solution over AW0.01 with the addition of isopropanol, benzoquinone, and Na_2- EDTA, respectively.

Furthermore, reactive species trapping experiments were conducted to understand the roles that the reactive species play in the photocatalytic process. It is well known that BZQ,Na_2-EDTA and tert-butanol are usually used as the radical scavengers for $O_2^{-\bullet}$ radicals, holes and •OH,[28] respectively. Therefore, these reagents were put into the photocatalytic system respectively before the experiments began. When tert-butanol is added, the degradation time does not change, which implies there is no occurrence of •OH radicals during the photocatalytic process. The degradation of RhB is not dramatically inhibited by the addition of a $O_2^{-\bullet}$ radical scavenger, BZQ. However, Na_2-EDTA can lead to an extension of degradation time. RhB can be degraded 30% in 9 min after the addition of Na_2-EDTA, which means that the holes play the main roles in the oxidization of RhB (Fig.7). The valence band edge potential of Ag_3PO_4 is 2.45 eV, less positive than E^{Θ} ($OH\cdot/H_2O$) (2.68 eV).Therefore, the photogenerated holes cannot directly oxidize the adsorbed H_2O into OH· radicals. The $E^{\Theta}(O_2/O_2^{-\bullet})$ (0.13 eV) [29]is more negative than the conduction band edge potential of Ag_3PO_4, which indicates that the formation of $O_2^{-\bullet}$ radicals via the reduction of O_2 by photogenerated electrons is excluded. Therefore, the decomposition of RhB is achieved by h^+ oxidation.

Mechanism of the improved photocatalytic activity of the as-prepared Ag_3PO_4 /WS_2 composites

The theoretical potentials of the valance bands of WS_2 and Ag_3PO_4 are 2.11eV and 2.9eV (VS NHE), respectively [30-32]. Therefore, the corresponding potentials of their conduction bands can be determined to be 0.21 and 0.45eV. Because of the energy level match between Ag_3PO_4 and WS_2, the transfer of the electrons from WS_2 to Ag_3PO_4 is encouraged, whereas the holes located in the valance band of Ag_3PO_4 are prone to migrate to the valance band of WS_2. Consequently, the photogenerated electrons and holes are separated (Fig.8). Furthermore, compared with pure Ag_3PO_4, the multi-interface Ag_3PO_4/WS_2 composite has the merits of high interface area, abundant active sites, wider space charge region, and reduced path length of charge transmission.

Therefore these synergistic properties allow more efficient separation of carriers, leading to higher photocatalytic activity.

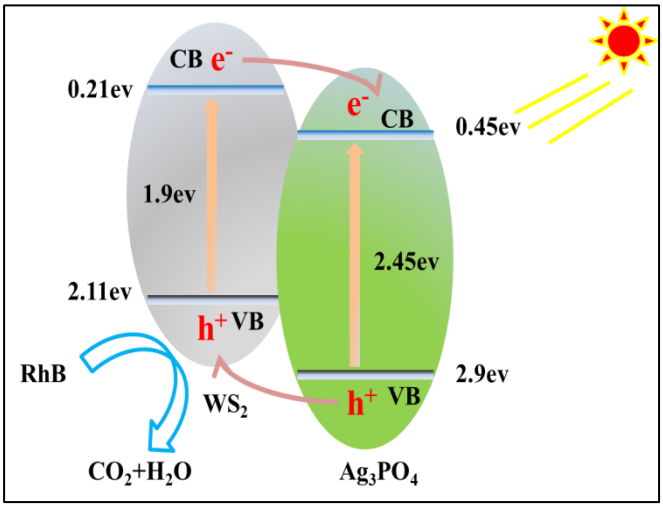

Fig.8 Schematic of band structure and expected charge separation of Ag_3PO_4/WS_2 composites under visible-light irradiation.

In summary, three factors are responsible for the improved performance of Ag_3PO_4 induced by WS_2. First, the WS_2 sheets show strong infinity to the RhB dyes. Second, the close contact between the two compounds can protect nano Ag_3PO_4 from detaching, which maintains the activity and stability of Ag_3PO_4. Lastly, the energy level match between Ag_3PO_4 and WS_2 and the multi-interface effect inhibit the recombination of photo-generated carriers and improve the photocatalytic activity of Ag_3PO_4.

Conclusions

To summarize, Ag_3PO_4/WS_2 composite photocatalysts have been successfully fabricated by controlling growth of Ag_3PO_4 nanoparticles within WS_2 sheets. The uncoordinated S atoms on the WS_2 sheets play an important role in regulating the microstructure and composition of the Ag_3PO_4/WS_2 composite. The energy level match between Ag_3PO_4 and WS_2 and the multi-interfaces effect encourage the charge separation, leading to higher photocatalytic activity of Ag_3PO_4/WS_2 composite than pure Ag_3PO_4. The close contact of WS_2 sheets with Ag_3PO_4 reduces the dissolving rate of Ag^+ from Ag_3PO_4 into water, thereby improving the stability of Ag_3PO_4.

Acknowledgements

This work was financially supported by Fundamental Research Funds for the Central Universities (WUT: 2015IB002), the National Natural Science Foundation of China (51161140399) and the Ministry of Science and Technology of China (2015DFR50650).

Notes and references

1. O. Sacco, V. Vaiano, C. Han, D. Sannino and D. D. Dionysiou, *Appl Catal B-Environ*, 2015, **164**, 462-474.
2. H. Yaghoubi, Z. Li, Y. Chen, H. T. Ngo, V. R. Bhethanabotla, B. Joseph, S. Q. Ma, R. Schlaf and A. Takshi, *Acs Catal*, 2015, **5**, 327-335.
3. M. Zhu, P. Chen and M. Liu, *Acs Nano*, 2011, **5**, 4529-4536.
4. Z. G. Yi, J. H. Ye, N. Kikugawa, T. Kako, S. X. Ouyang, H. Stuart-Williams, H. Yang, J. Y. Cao, W. J. Luo, Z. S. Li, Y. Liu and R. L. Withers, *Nature materials*, 2010, **9**, 559-564.
5. Y. Bi, S. Ouyang, N. Umezawa, J. Cao and J. Ye, *J Am Chem Soc*, 2011, **133**, 6490-6492.
6. Z. H. Chen, W. L. Wang, Z. G. Zhang and X. M. Fang, *J Phys Chem C*, 2013, **117**, 19346-19352.
7. X. G. Ma, B. Lu, D. Li, R. Shi, C. S. Pan and Y. F. Zhu, *J Phys Chem C*, 2011, **115**, 4680-4687.
8. X. F. Yang, H. Y. Cui, Y. Li, J. L. Qin, R. X. Zhang and H. Tang, *Acs Catal*, 2013, **3**, 363-369.
9. H. Katsumata, T. Sakai, T. Suzuki and S. Kaneco, *Ind Eng Chem Res*, 2014, **53**, 8018-8025.
10. H. Zhu, C. Xiao, H. Cheng, F. Grote, X. D. Zhang, T. Yao, Z. Li, C. M. Wang, S. Q. Wei, Y. Lei and Y. Xie, *Nat Commun*, 2014, **5**.
11. X. L. Zheng, J. B. Xu, K. Y. Yan, H. Wang, Z. L. Wang and S. H. Yang, *Chem Mater*, 2014, **26**, 2344-2353.
12. K. Komori and N. Umehara, *Tribol Int*, 2015, **84**, 100-109.
13. Q. Li, N. Zhang, Y. Yang, G. Z. Wang and D. H. L. Ng, *Langmuir*, 2014, **30**, 8965-8972.
14. S. Jo, N. Ubrig, H. Berger, A. B. Kuzmenko and A. F. Morpurgo, *Nano Lett*, 2014, **14**, 2019-2025.
15. X. Zong, H. Yan, G. Wu, G. Ma, F. Wen, L. Wang and C. Li, *J Am Chem Soc*, 2008, **130**, 7176-7177.
16. L. Hu, Y. Ren, H. Yang and Q. Xu, *ACS Appl Mater Interfaces*, 2014, **6**, 14644-14652.
17. S. Ratha and C. S. Rout, *ACS Appl Mater Interfaces*, 2013, **5**, 11427-11433.
18. J. N. Coleman, M. Lotya, A. O'Neill, S. D. Bergin, P. J. King, U. Khan, K. Young, A. Gaucher, S. De, R. J. Smith, I. V. Shvets, S. K. Arora, G. Stanton, H. Y. Kim, K. Lee, G. T. Kim, G. S. Duesberg, T. Hallam, J. J. Boland, J. J. Wang, J. F. Donegan, J. C. Grunlan, G. Moriarty, A. Shmeliov, R. J. Nicholls, J. M. Perkins, E. M. Grieveson, K. Theuwissen, D. W. McComb, P. D. Nellist and V. Nicolosi, *Science*, 2011, **331**, 568-571.
19. Z. Chen, S. Q. Liu, M. Q. Yang and Y. J. Xu, *Acs Appl Mater Inter*, 2013, **5**, 4309-4319.
20. C. Nethravathi, A. A. Jeffery, M. Rajamathi, N. Kawamoto, R. Tenne, D. Golberg and Y. Bando, *Acs Nano*, 2013, **7**, 7311-7317.
21. X. J. Guan and L. J. Guo, *Acs Catal*, 2014, **4**, 3020-3026.
22. Y. Yan, B. Y. Xia, X. M. Ge, Z. L. Liu, J. Y. Wang and X.

Wang, *Acs Appl Mater Inter*, 2013, **5**, 12794-12798.
23. S. Ratha and C. S. Rout, *ACS Appl Mater Interfaces*, 2013, **5**, 11427-11433.
24. Y. M. He, L. H. Zhang, B. T. Teng and M. H. Fan, *Environmental science & technology*, 2015, **49**, 649-656.
25. J. W. Xu, Z. D. Gao, K. Han, Y. M. Liu and Y. Y. Song, *Acs Appl Mater Inter*, 2014, **6**, 15122-15131.
26. Y. Y. Bu and Z. Y. Chen, *Acs Appl Mater Inter*, 2014, **6**, 17589-17598.
27. P. Ma, A. Chen, Y. Wu, Z. Fu, W. Kong, L. Che and R. Ma, *J Colloid Interface Sci*, 2014, **417**, 293-300.
28. Z. Z. Lou, B. B. Huang, Z. Y. Wang, X. C. Ma, R. Zhang, X. Y. Zhang, X. Y. Qin, Y. Dai and M. H. Whangbo, *Chem Mater*, 2014, **26**, 3873-3875.
29. M. Ge, N.Zhu, Y.P. Zhao, J. Li, and L. Liu, *Ind. Eng. Chem. Res.* 2012, **51**, 5167−5173.
30. L. Y. Gan, Q. Y. Zhang, Y. C. Cheng and U. Schwingenschlogl, *J Phys Chem Lett*, 2014, **5**, 1445-1449.
31. W. F. Yao, B. Zhang, C. P. Huang, C. Ma, X. L. Song and Q. J. Xu, *J Mater Chem*, 2012, **22**, 4050-4055.
32. J. J. Guo, H. Zhou, S. X. Ouyang, T. Kako and J. H. Ye, *Nanoscale*, 2014, **6**, 7303-7311.